RESEARCH ARTICLE

Flow features of underexpanded microjets emerging from a round convergent nozzle

Tenta Tashiro[1] · Ryota Fukunaga[1] · Daisuke Utsunomiya[1] · Shinichiro Nakao[1] · Yoshiaki Miyazato[1] · Yojiro Ishino[2]

Abstract

Density measurements of underexpanded microjets that emerge from a round convergent nozzle with an inner diameter of 1 mm at the exit are taken using rainbow schlieren deflectometry to nonintrusively capture an extensive region from the nozzle exit to a downstream location of twenty times the nozzle exit diameter. Flow visualizations of the microjets are carried out at nozzle pressure ratios (NPRs) of 3.0, 4.0, 5.0, 6.0, and 7.0 and corresponding fully expanded jet Mach numbers (M_j) of 1.36, 1.56, 1.71, 1.83, and 1.93, where the NPR can be defined as the ratio of the stagnation pressure upstream of the nozzle to the back pressure. The three-dimensional density fields of the microjets are reconstructed at a spatial resolution of approximately 4 μm by the Abel inversion technique based upon the assumption of axisymmetric density fields. The flow topology of the near-field shock structure for each NPR is demonstrated with an elevated view of the density field, including the jet central axis. The location and flow Mach number of the first local minimum in the density profile along the jet central axis are experimentally provided for the first time as a function of the NPR to propose an empirical relation. An approximate expression for the flow Mach number on the jet central axis from the nozzle exit to the location where the isentropic process is established is also derived against the streamwise distance. In addition, the supersonic length of a shock-containing microjet, which is defined as the distance along the jet central axis from the nozzle exit to the location farthest downstream at which there exists a local flow Mach number of unity, is acquired from the density profile along the jet centerline and compared quantitatively with the experimental data from previous Pitot probe surveys as well as previous empirical relations. Furthermore, the microjet density fields from rainbow schlieren deflectometry are mutually compared with those from previous Mach–Zehnder interferometry under the same nozzle to investigate the effects of nonintrusive techniques on the density profiles along three representative locations: the jet centerline, intermediate line, and lipline.

1 Introduction

There is significant interest in studying supersonic microjets due to their numerous applications, including the aerodynamic extraction of fine foreign particles from the surface of a substrate (Smedley et al. 1999), the active control of flow separation in a diffuser (Kumar and Alvi 2006), jet noise suppression (Alkislar et al. 2007), and the micro-propulsion of small satellites (Louwerse et al. 2009). To the best of our knowledge, the first extensive experimental study of supersonic microjets emerging from round nozzles was performed by Scroggs and Settles (Scroggs and Settles 1996), who used

Ryota Fukunaga, Daisuke Utsunomiya, Shinichiro Nakao, Yoshiaki Miyazato, and Yojiro Ishino contributed equally to this work.

✉ Yoshiaki Miyazato
  miyazato@kitakyu-u.ac.jp

  Tenta Tashiro
  tenta.tashiro21@gmail.com

  Ryota Fukunaga
  ryota090808@gmail.com

  Daisuke Utsunomiya
  007.daino.821@gmail.com

  Shinichiro Nakao
  s-nakao@kitakyu-u.ac.jp

  Yojiro Ishino
  evg97234@ict.nitech.ac.jp

[1] Department of Mechanical Systems Engineering, The University of Kitakyushu, 1-1 Hibikino, Wakamatsu-ku, Kitakyushu 808-0135, Japan

[2] Department of Mechanical Engineering, Nagoya Institute of Technology, Gokiso-cho, Showa-ku, Nagoya 466-8555, Japan

the schlieren technique to qualitatively visualize microjet structures. In addition, they carried out Pitot probe surveys along the jet centerline from the nozzle exit to a downstream location of several tens of times the nozzle exit diameter. By analyzing these experimental data, they acquired the supersonic lengths of microjets under the overexpanded, correctly expanded and underexpanded conditions since it is one of the primary flow quantities for examining supersonic free jets. However, as described later, it is often seen that the technical term referred to as supersonic length has been used in a confusing manner. Hence, we first describe the definition of this technical term because it is not well defined even in a recent review paper (Franquet et al. 2015) on supersonic free jets.

It has been widely recognized that there are four representative lengths to characterize supersonic jets: the shock-cell length (Love et al. 1959; Tam 1995) (often called the shock-cell spacing), the potential core length (Nagamatsu et al. 1969; Lau et al. 1979; Morrison and McLaughlin 1980; Hileman and Samimy 2006), the supersonic core length (Nagamatsu et al.1969; Rathakrishnan 2019; Kaushik 2019), and the supersonic length (Nagamatsu et al. 1969; Scroggs and Settles 1996). The shock-cell length, L_s, can be determined from schlieren pictures as the distance from the nozzle exit to the point where the reflected shock intersects the jet boundary (Love et al. 1959). However, this definition of length can be accompanied by some errors because the location of the jet boundary may be ambiguous. Instead, L_s can also be experimentally defined as the distance between the first successive peaks of maximum or minimum flow properties such as velocities (Saddington et al. 2004), Pitot pressures (Phalnikar et al. 2008), and densities (Nagata et al. 2022) along the centerline in the core region of the jet. The normalized shock-cell length is analytically given (Tam and Tanna 1982; Nagata et al. 2022) through

$$\frac{L_s}{D_e} = \frac{\pi\sqrt{M_j^2 - 1}}{2.405}\sqrt{\frac{M_d}{M_j}}\left[\frac{(\gamma-1)M_j^2 + 2}{(\gamma-1)M_d^2 + 2}\right]^{\frac{\gamma+1}{4(\gamma-1)}} \tag{1}$$

where D_e is the inner diameter of the nozzle exit, γ is the specific heat ratio, M_d is the nozzle design Mach number, and M_j is the fully expanded flow Mach number. The fully expanded flow Mach number is related to the nozzle pressure ratio (NPR = p_{os}/p_b) of the stagnation pressure (p_{os}) upstream of the nozzle to the back pressure (p_b), as follows:

$$M_j = \sqrt{\frac{2}{\gamma-1}\left(\text{NPR}^{\frac{\gamma-1}{\gamma}} - 1\right)} \tag{2}$$

The potential core length (Nagamatsu et al. 1969; Lau et al. 1979; Morrison and McLaughlin 1980; Hileman and Samimy 2006), L_p, can be estimated only when the static pressure at the nozzle exit is equal to the back pressure (i.e.,

the ideally expanded condition or nozzle design condition), which can be defined as the axial distance from the nozzle exit to the location where the centerline velocity is the same as the nozzle exit velocity and estimated as the intersection of lines that are fitted to the uniform velocity and linear decrease regions of centerline flow quantities such as the velocity values and Pitot pressures. Therefore, neither shock-loss in the shock-cells nor mixing-loss between the jet and ambient fluid occurs along the jet central axis from the nozzle inlet to the end of the potential core. The normalized potential core length suggested by Lau et al. (1979) can be empirically given as

$$\frac{L_p}{D_e} = 4.2 + 1.1M_j^2 \tag{3}$$

Nagamatsu et al. (1969) defined the supersonic core length, L_c, for underexpanded jets as the distance from the nozzle exit to the location on the axis where the initial jet velocity still exists. The normalized supersonic core length is given as

$$\frac{L_c}{D_e} = 5.22M_j^{0.9} + 0.22 \tag{4}$$

for various shock-containing jets, such as underexpanded jets issued from Laval nozzles and heated supersonic jets. Rathakrishnan (2019) defined L_c as the axial distance from the nozzle exit to the location at which the characteristic decay begins. It should be noted that L_c is the same as L_p for jets issuing from convergent or convergent-divergent nozzles operating at the design condition. Inside the supersonic core of underexpanded jets, shock-loss is included (Nagamatsu et al. 1969; Donaldson and Snedeker 1971), and the flow Mach number at the end of the supersonic core is generally beyond unity (Nagamatsu et al. 1969) for underexpanded jets emerging from Laval (supersonic) nozzles. Saddington et al. (2004) defined the supersonic core length (called the shock core length in their paper) as the axial distance from the nozzle exit to the end of the last shock-cell. In any of the above definitions, L_c is determined with ambiguity.

The supersonic length, L^*, in the present study is defined as the streamwise distance along the jet central axis from the nozzle exit to the location farthest downstream at which there exists a local flow Mach number of unity (Shirie and Seubold 1967). This length was initially defined by Shirie and Seubold (1967) as the supersonic core length. Later, Nagamatsu et al. (1969) referred to it as the supersonic length and empirically derived it as

$$\frac{L^*}{D_e} = 5M_j^2 + 0.8 \tag{5}$$

for macroscale supersonic jets (Nagamatsu et al. 1969).

In recent studies on supersonic microjets (Phalnikar et al. 2008; Aniskin et al. 2013, 2015; Mironov et al. 2019; Perumal and Rathakrishnan 2021), the term "supersonic core length" has been used instead of "supersonic length" defined in this paper. As seen from Eqs. (4) and (5), these lengths are completely different characteristic quantities from each other. Saddington et al. (2004) obtained results of $L_c/D_e = 7.5$ and $L*/D_e = 10.8$ from the RANS simulation with the renormalization group (RNG) $k - \epsilon$ turbulence model for an underexpanded sonic jet of NPR = 2.5. Therefore, to prevent confusion, we adopt the definition of Nagamatsu et al. (1969) for L^* hereafter. If the term supersonic core length is used in the sense of the supersonic length in the papers cited in this study, we rewrite the supersonic core length to the supersonic length without any explanation.

To the best of the authors' knowledge, supersonic lengths of shock-containing microjets were obtained for the first time by Scroggs and Settles (1996), who estimated L^* from schlieren pictures based on the assumption that the refractive index of light changes along the boundaries of the supersonic region and found that L^* can be correlated well with Eq. (5). Since then, many researchers have investigated the supersonic lengths of supersonic microjets through conventional schlieren visualization as well as micro-Pitot probe surveys (Phalnikar et al. 2008; Aniskin et al. 2013, 2015; Mironov et al. 2019; Perumal and Rathakrishnan 2021). Phalnikar et al. (2008) experimentally examined underexpanded microjets issuing from axisymmetric convergent nozzles with exit diameters from 100 μm to 1000 μm. They observed the microjet structures using a micro-schlieren system with high magnification and performed micro-Pitot probe surveys to measure the jet decay, jet spreading rate, shock-cell spacing, and supersonic length. They concluded that the supersonic lengths for microjets are lower than those for macrojets due to the stronger viscous effects associated with microjets operating at relatively low Reynolds numbers. They derived an empirical relation for L^* as follows:

$$\frac{L^*}{D_e} = 1.8\,\text{NPR} + 2.9 \tag{6}$$

for microjets emerging from convergent nozzles with inner diameters of 200 μm and 400μm at the exit. Aniskin et al. (2013, 2015) investigated supersonic nitrogen microjets issuing from round convergent nozzles with exit diameters of 10.4 μm to 341 μm, in which a micro-Pitot tube with an intake hole of 12 μm in diameter was fabricated, and the Pitot pressures along the centerline of shock-containing microjets were measured to investigate the effects of Reynolds numbers on the shock-cell spacing and supersonic length. They showed that the supersonic lengths of

microjets emerging from convergent nozzles with exit diameters of 10.4 μm and 16.1 μm are much longer than those of macrojets.

Most recently, Perumal and Rathakrishnan (2021) presented empirical relations for the supersonic length in round and elliptic shock-containing jets, which include the equivalent diameter of the nozzle throat, the design Mach number, the aspect ratio at the nozzle exit, and the nozzle pressure ratio as governing parameters. Regarding free jets emerging from round convergent nozzles ($M_d = 1$), the normalized supersonic length can be expressed by

$$\frac{L^*}{D_e} = e^{0.11\gamma M_j^2}\left(-0.226\text{NPR}^2 + 2.87\text{NPR} + 0.03\right) \tag{7}$$

Conventional schlieren techniques can provide qualitative flow features only (Settles 2001). In addition, the insertion of any intrusive probe such as the Pitot tube or the hot-wire probe into the shock-containing flows changes the shock structure significantly. Although particle-based velocimetries, including laser Doppler anemometry (LDA) and particle image velocimetry (PIV), are effective techniques that can be used to investigate large-scale free jets, the application for shock-containing microjets remains questionable due to inadequate seeding and velocity slip errors just behind the shocks (Sakurai et al. 2015; Feng and McGuirk 2016; Wernet 2016; Yüceil 2017). Hence, even for round supersonic microjets, the detailed flow structures are yet to be fully understood because of challenging issues. On the other hand, the near-field region of shock-containing microjets can be measured through schlieren-based quantitative visualizations and laser interferometry. For instance, to the best of the authors' knowledge, Kolhe and Agrawal (2009) applied rainbow schlieren deflectometry (RSD) (Agrawal and Wanstall 2018) to shock-containing microjets for the first time. They showed that the RSD can provide high-quality quantitative data to explain the detailed structure of underexpanded microjets issuing from an orifice injector of 500 μm. Nazari et al. (2020) experimentally investigated shock-containing microjets issuing from round and square Laval nozzles with a design Mach number of 1.5 using the calibrated schlieren. They developed a twenty-directional quantitative schlieren system with flashlight sources to capture the instantaneous three-dimensional density field of shock-cell structures under overexpanded, ideally expanded, and underexpanded conditions. In addition, the shock-cell spacing and supersonic length of supersonic microjets were shown against the nozzle pressure ratio.

Recently, Sugawara et al. (2020, 2021) experimentally clarified the fine structure of a shock-containing microjet issuing from a round convergent nozzle with an inner diameter of 1 mm at the exit by Mach–Zehnder interferometry (MZI). In addition, they simulated by solving the

Reynolds-averaged Navier–Stokes (RANS) equations with the Menter's shear stress transport (SST) $k - \omega$ turbulence model to investigate the near-field structure of the shock-containing microjet. In the present work, we pay particular attention to the flow features in the near-field region and the supersonic length for underexpanded microjets emerging from a round convergent nozzle under a range of NPRs from 3.0 to 7.0. The RSD is utilized to acquire a wide range of density fields of the microjets from the nozzle exit to a downstream distance of twenty times the nozzle exit diameter. Moreover, we advance the fundamental understanding of the shock-containing microjets and provide a database that can be used for the validation of the computational codes. In addition, the near-field density fields captured by the RSD are quantitatively compared with those captured by the MZI (Sugawara et al. 2020, 2021) under the same nozzle to clarify the differences between the measurement techniques.

Following the introduction in Sect. 1, the experimental setup including a test nozzle and rainbow schlieren optical system is described in Sect. 2. The density fields captured by the RSD are presented with comparisons to previous experimental data and empirical relations in Sect. 3. Finally, the conclusions with future perspectives are provided in Sect. 4.

2 Experimental methods

2.1 Measurement systems and test nozzle

The experiments were conducted in an intermittent blowdown compressed-air facility in the High-Speed Gasdynamics Laboratory at the University of Kitakyushu. Since the facility has been described in detail elsewhere (Takano et al. 2016; Fukunaga et al. 2022; Nagata et al. 2022), only a brief description is given in the present paper. Ambient air is pressurized by the compressor up to 1 MPa and stored in a high-pressure reservoir comprising two storage tanks with a total capacity of 2 m^3 after filtering and drying. The supply line from the reservoir can be connected to the plenum chamber through coupling, as shown in Fig. 1. Hence, the high-pressure dry air from the reservoir stagnates in the plenum chamber. Subsequently, it is discharged into the atmosphere through a test nozzle that can be rotated about its central axis (Takano et al. 2016) if necessary, as in taking the multi-viewing schlieren pictures of asymmetric density fields (Fukunaga et al. 2022). The desired NPR (p_{os}/p_b) is achieved by changing the plenum pressure, p_{os}, because the back pressure, p_b (= atmospheric pressure), is constant.

As shown in Fig. 2, a round convergent nozzle with inner diameters of 6 mm and 1 mm at the inlet and exit, respectively, which is the same nozzle as that described
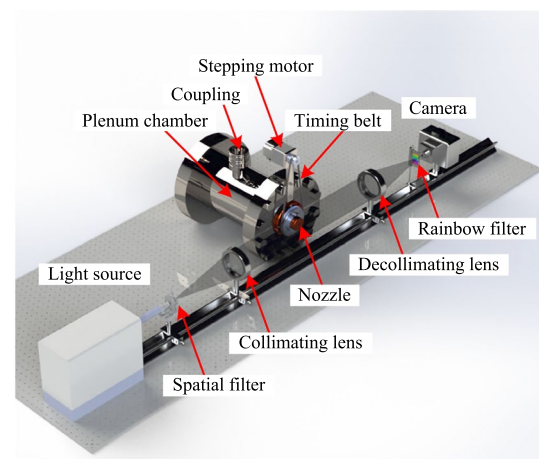

Fig. 1 Schematic diagram of the blowdown compressed-air facility with a rainbow schlieren optical system. A test nozzle is attached to the plenum chamber with a pulley that can be rotated about its central axis using a stepping motor through a timing belt. The supply line from the reservoir can be connected to the plenum chamber through coupling. A rainbow filter is introduced into the schlieren cutoff plane just before the camera
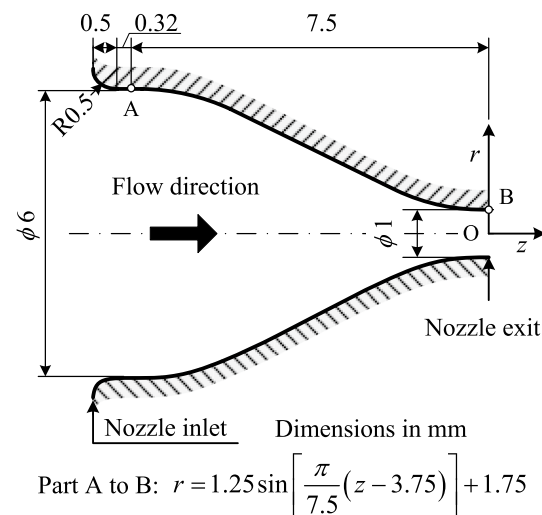

Fig. 2 Schematic drawing of a round convergent nozzle with a 1 mm diameter at the exit. The nozzle wall contour from the inlet to the exit is designed based on a sinusoidal curve to provide smooth uniform and parallel flows at the inlet and exit. The nozzle has a lip thickness of 1.5 mm at the exit. All dimensions are in mm

by Sugawara et al. (2020, 2021), was used as the test nozzle. The nozzle wall contour from the inlet to the exit was designed based on a sinusoidal curve to provide smooth uniform flows at the inlet and exit. In addition, the nozzle has a lip thickness of 1.5 mm at the exit, which would be an important parameter that strongly affects the flow structure. The nozzle was manufactured from a brass block using a

cut-processing machine (Kitamura Machinery, Mycenter-3XG) with a positioning accuracy of ± 2 μm and a repeatability of ± 1 μm. To estimate the error of circularity for the wall shape at the nozzle exit section, we obtained a digital image of the nozzle exit section by laser scanning microscopy (Olympus, LEXT OLS4100) (Sugawara et al. 2021). After reading the image in a personal computer, the radial distances from a certain reference point to the wall periphery were measured at each angle of 20 deg around the reference point with AutoCAD2013 software. The precision error for the radius of the least-squares circle becomes ± 1.4 μm, which corresponds to approximately ± 0.3 % of the radius.

2.2 Rainbow schlieren deflectometry

As shown in Fig. 1, the jet flow fields were visualized through rail-mounted optical components, including a spatial filter with a rectangular source aperture of 3 mm in height $\times 50$ μm in width; two achromatic lenses with a diameter and focal length of 100 mm and 500 mm, respectively; a rainbow filter with a continuous hue variation at a width of 2.4 mm; and a digital camera (Nikon D7100, 6000×4000 square pixel resolution with a 14-bit pixel depth) fitted with a focusing lens with a diameter and focal length of 30 mm and 600 mm, respectively. A continuous 250-W metal halide light source (Sigmakoki, IMH-250) connected to a fiber optic cable with a diameter of 50 μm provided light input to the spatial filter through an objective lens with a focal length of 16.56 mm. The rainbow filter was introduced into the back focal plane (schlieren cutoff plane) of the decollimating lens horizontally with respect to the nozzle axis. This filter setting corresponds to the horizontal knife edge in the conventional schlieren system. Moreover, the width of the source aperture was perpendicular to the nozzle axis to measure the deflection angle in the horizontal direction.

The camera outputs of rainbow schlieren images in RGB format were transferred onto a personal computer hard drive using Nikon Camera Control Pro software and then stored as JPEG files. Each JPEG RGB image (8-bit each) was turned into an HSI image (8-bit each) according to the hue (H)-saturation (S)-intensity (I) representation obtained from direct transformation of the RGB tristimulus values (Greenberg et al. 1995). Only the transformed hue (H) values were utilized to calculate the ray shift (d) at the cutoff plane of the schlieren system. This indicates that a unique hue can be transmitted to the image plane from a given location on the filter plane (Greenberg et al. 1995). Thus, the ray shift on the filter plane could be related to the hue measured in the image plane. This color representation eliminates numerous problems associated with the inhomogeneous absorption or scattering of light by the medium, nonlinearities in recording

the image, intensity fluctuations of the source, and so on (Greenberg et al. 1995; Al-Ammar et al. 1998).

An in-house rainbow filter with 2.4 mm in width by 35 mm in height was utilized in the present study. An image of the rainbow filter is shown with the calibration curve in Fig. 3. In the HSI color representation, the hue (color) of the rainbow filter changes continuously from the left to right ends, and a physical quantity from 0 to 360 degrees is assigned to the hue at each position. The more detailed explanation about how to design and generate a rainbow filter can be found in Agrawal and Wanstall (2018). The rainbow filter was calibrated by moving it perpendicular to
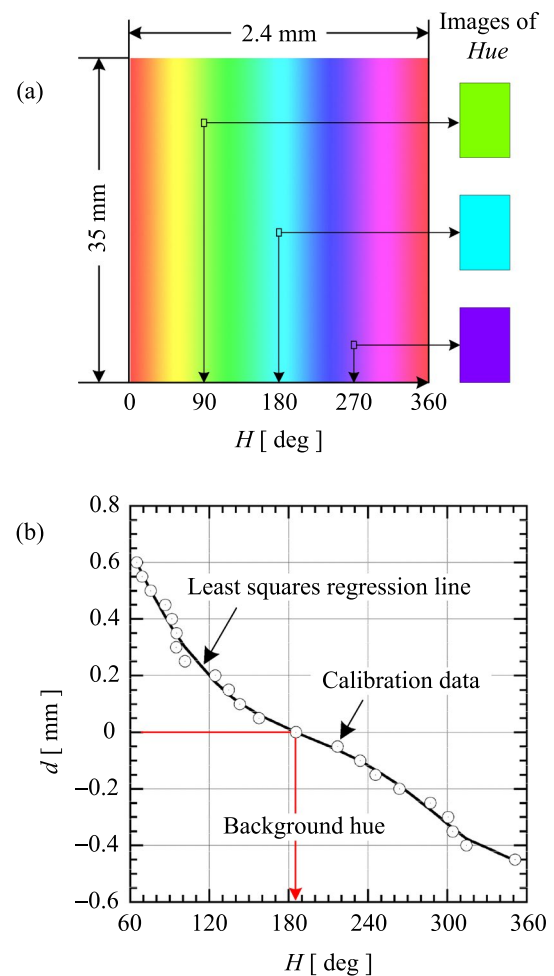

Fig. 3 The calibration characteristics of a rainbow filter. **a** An image of a rainbow filter with representative hues in $H = 90$, 180, and 270 degrees and **b** the filter calibration characteristics. The filter calibration was performed by moving the filter at steps of 10 μm in the schlieren cutoff plane before starting experiments. The open symbols denote calibration data and a fifth-order polynomial curve fitting is utilized as least squares regression. The background hue corresponds to $H =$ approximately 185 deg

the nozzle axis in intervals of 10 μm just before starting the experiments. The open symbols express the experimental data with a maximum precision error of approximately 1 deg on the hue values. The solid line indicates a least squares regression line of the calibration data, which is given by a fifth-order polynomial. The background hue in the rainbow filter for the present experiment corresponds to the location shown as the red arrow.

The schlieren pictures of the microjets were taken with an exposure time of 1/500 s and ISO 1000 with a continuous schlieren light source for a fixed NPR. The center of the jet was in focus. The spatial resolution of the present rainbow schlieren system was 3.8 μm in the object plane. Five schlieren images were recorded for each NPR to estimate statistical information such as the average and standard deviation. In this study, the density fields of underexpanded microjets were visualized over a range of NPRs from 3.0 to 7.0 in steps of 1.0 within an accuracy of $\pm$ 1.0 %. The total temperature in the plenum chamber was equal to room temperature (T_b = 298.4 K) within an accuracy of approximately 0.1 °C during the experiment. The p_b was 101.1 kPa $\pm$ 0.5 kPa. In the present study, the three-dimensional density fields of the underexpanded microjets were reconstructed using the Abel inversion method based upon the assumption of axisymmetric density fields. A detailed description of the reconstruction process is given in Maeda et al. (2018).
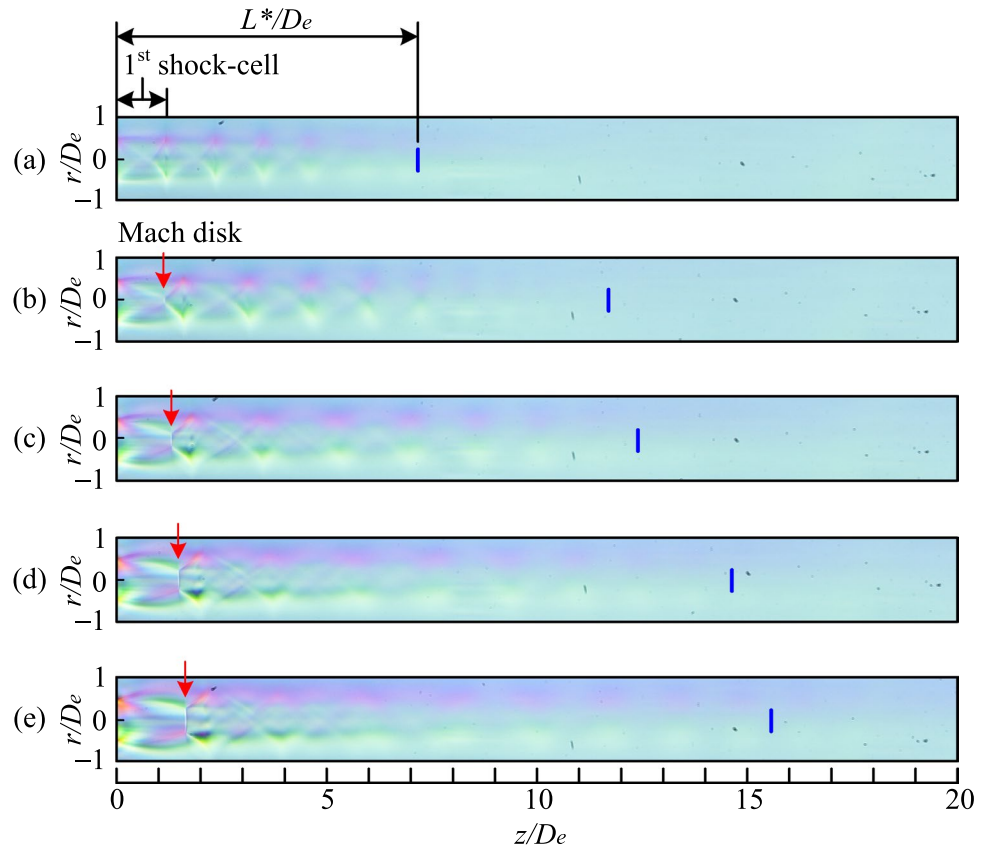
3 Results and discussion

3.1 Rainbow schlieren pictures

Typical rainbow schlieren pictures with the horizontal setting of a rainbow filter are shown in Fig. 4a through 4e, which exhibit density gradients perpendicular to the jet central axis and averaged in the viewing direction. The flow direction is from left to right. The horizontal (z) and vertical (r) axes are normalized by the nozzle exit diameter D_e. Since a round convergent nozzle is used in this study, the design Mach number is unity, and the design nozzle pressure ratio is approximately 1.89 for γ = 1.4. Therefore, all jets observed in the present experiments are underexpanded.

For NPR = 3, the shocks in the jet plume are very weak, and hence, a typical shock-cell structure generated by repeating a series of expansion and compression zones can be clearly observed in the near-field region until at least z/D_e = 5. No Mach disk can be seen in the first shock-cell. In Fig. 4a, the blue short vertical line, which is at z/D_e = approximately 7, denotes the end location of the supersonic region in the jet centerline. This is determined from the jet centerline density profile in Sect. 3.3, as described later, and is given as the normalized supersonic length L^*/D_e. No significant flow structure can be

Fig. 4 Rainbow schlieren pictures of underexpanded sonic jets for **a** NPR = 3, **b** NPR = 4, **c** NPR = 5, **d** NPR = 6, and **e** NPR = 7. The rainbow filter is set up horizontally with respect to the jet axis in the cutoff plane. The location of a Mach disk is shown as the red downward arrow. The short blue vertical line in each figure indicates the end location of the supersonic region in the jet centerline

seen further downstream of the supersonic region. When the NPR increases to 4, as shown in Fig. 4b, a Mach disk with a very small diameter appears in the first shock-cell and its streamwise location is shown as the red downward arrow. Further increases from NPR = 5 to 7 lead to an increase in the Mach disk diameter and move the Mach disk downstream direction.
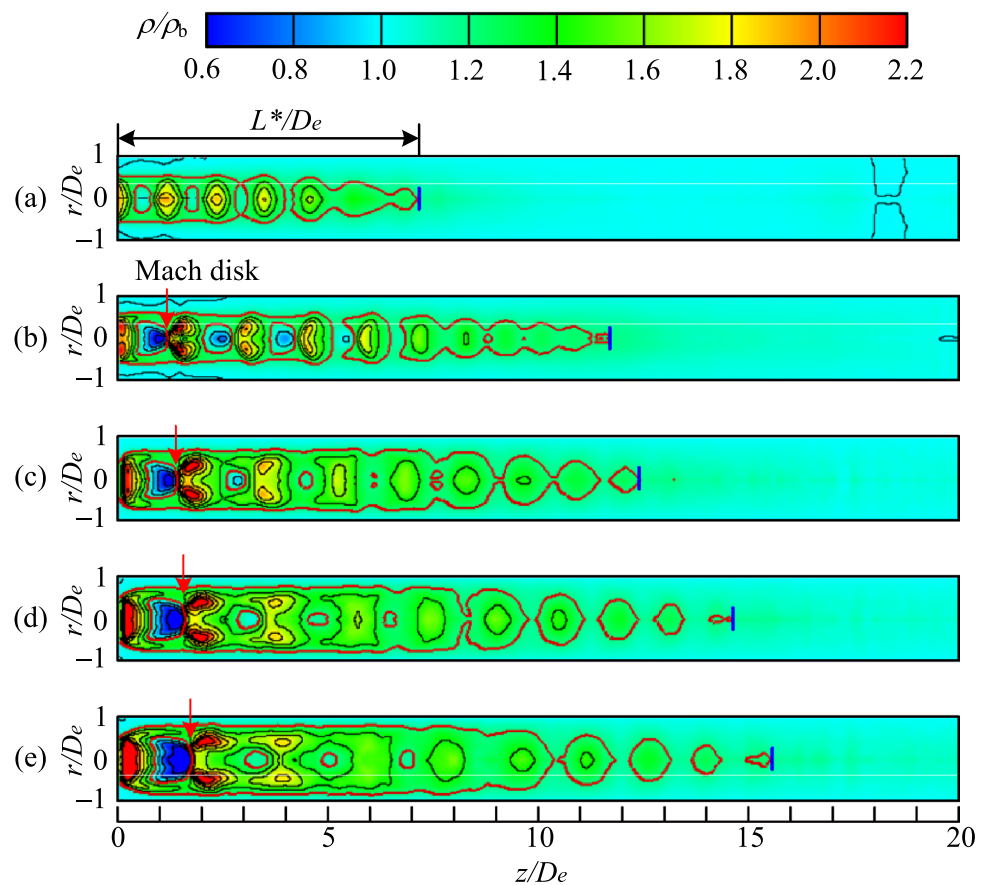
In the past, Love et al. (1959) experimentally showed that a Mach disk is produced within the first shock-cell of an underexpanded sonic jet when the ratio p_e/p_b of the nozzle exit pressure to the back pressure is greater than approximately 2, which corresponds to NPR = 3.78. Other past studies reported that a Mach disk is formed at NPR = 3.9 (Crist et al. (1966)), 3.47 (Gibbings et al. (1972)), and 3.8 (Powell (1988)). The most recent numerical study by Muraoka and Hiejima (2022) indicates that a Mach disk occurs between NPR = 3.03 and 3.12. On the other hand, Sugawara et al. (2020, 2021) applied the MZI for microjets emerging from the same nozzle as the present study to acquire the density fields and found that a Mach disk occurs for NPR = 4, but not for NPR = 3. However, Hornung (2000), Gribben et al. (2000), and Hornung and Schwendeman (2001) state that, in an axisymmetric supersonic jet, there must always be a Mach reflection at the central axis of the jet, i.e., a Mach disk must always be produced in axisymmetric free jets, which is

simply a question of how small it is. The issue of whether a Mach disk always occurs is a subject for our future research.

3.2 Two-dimensional density fields

The two-dimensional density fields on the cross section including the jet centerline for NPRs from 3.0 to 7.0 in steps of 1.0 are illustrated in Fig. 5 with the flow from left to right. The density fields are normalized by the ambient density ρ_b, the contour levels with an interval of 0.2 are shown in the color bar at the top of Fig. 5, and the spatial resolution in the density map is approximately 4 μm. The radial and streamwise distances are normalized by D_e. The red solid lines seen in each figure indicate a contour with $\rho/\rho_b = 1.2$, and its most downstream location along the jet centerline is shown as the blue short vertical line, showing a location where the flow Mach number is equal to unity, i.e., the end location of the supersonic region. The red downward arrow in all figures except for Fig. 5a represents the Mach disk location. It is notable that the density fields shown here are not averaged over the width of the jet, but on the cross section including the central axis of the jet. An important point to emphasize is the fact that the jet density field in a cross section perpendicular to the viewing direction can be obtained with a spatial resolution of 4 μm. Therefore, these density

Fig. 5 Two-dimensional density contour plots including the jet central axis of underexpanded microjets emerging from a round convergent nozzle for **a** NPR = 3, **b** NPR = 4, **c** NPR = 5, **d** NPR = 6, and **e** NPR = 7. The radial and streamwise distances are normalized by the nozzle exit diameter. The density fields are normalized by the ambient density. The red solid line in each figure indicates a contour with $\rho/\rho_b = 1.2$, and the most downstream location along the jet centerline is shown as the blue short vertical line. The red downward arrow shows the Mach disk location on the jet central axis

fields can be utilized for validation by a direct comparison with numerical results.

Pitot tubes are very effective in investigating the flow characteristics along the jet central axis of a supersonic microjet (Phalnikar et al. 2008; Aniskin et al. 2013, 2015). However, intrusive probes such as Pitot tubes and hot-wire anemometry are not suitable for studying flow features in regions away from the central axis of the jet. In contrast, Fig. 5 clearly provides an overview of the jet structure over the entire region composed of the near-field zone where shock waves dominate and the subsequent far-field zone.

As shown in Fig. 5a, a microjet for NPR = 3 displays a typical shock-cell structure in which the expansion and compression regions sequentially repeat in the flow direction since the jet includes only weak shocks. The microjet is composed of a shock-cell structure with approximately the same geometrical shape. In Fig. 5b, when the NPR increases to 4, a Mach disk with a small diameter dimly appears in the first shock-cell. A short incident shock and its reflected shock occur at the triple points of the Mach disk in the first shock-cell. The local maxima in the density field are not produced along the jet central axis just behind the Mach disk; instead, they appear in the upper and lower zones sandwiched between the reflected shock and the expansion waves produced from the point at which the reflected shock intersects the jet free boundary. A similar phenomenon has been reported by Sugawara et al. (2020) for the density field of a microjet with a Mach disk. This peculiar phenomenon can be explained as follows. The ratio ρ_2/ρ_1 of the density ρ_2 just behind a normal shock to that ρ_1 just before the shock increases as the incoming Mach number just before the shock increases. However, the rate of increase gradually decreases as the Mach number increases, and eventually ρ_2/ρ_1 approaches a constant value of 6.0 at most for $\gamma =1.4$ and high Mach numbers (Saad 1993). As can be seen in Fig. 5b, the density is lowest just before the Mach disk, and the Mach number is highest there. On the other hand, near the jet boundary in front of the Mach disk, the density is higher and the Mach number is lower than that on the central axis of the jet. The strength of the reflected shock generated from the triple point of the Mach disk is weaker than that of the Mach disk, but the density value after passing through the former is higher than that after passing through the latter. This distinctive phenomenon can also be seen within the second shock-cell, suggesting the appearance of a second Mach disk, as shown in the numerical study of the jet by Edgington-Mitchell et al. (2014). In the past, Wernet (2016) applied the particle image velocimetry (PIV) to a heated underexpanded sonic jet issuing from a round convergent nozzle with an outlet diameter of 50.8 mm at NPR = 3.2 to discern a second Mach disk downstream of a first. However, in order to accurately predict the presence of the second Mach disk, information on the Mach numbers inside the jet is definitely needed. It should be noted that the shock strength would be weaker in the second Mach disk than in the first; therefore, the schlieren picture in Fig. 4b is not expected to recognize the second Mach disk. Spatial variations in the shock structure with an increase in NPR can be clearly observed from Fig. 5c,d ,e when compared with the corresponding schlieren pictures of Fig. 4c, d, e.
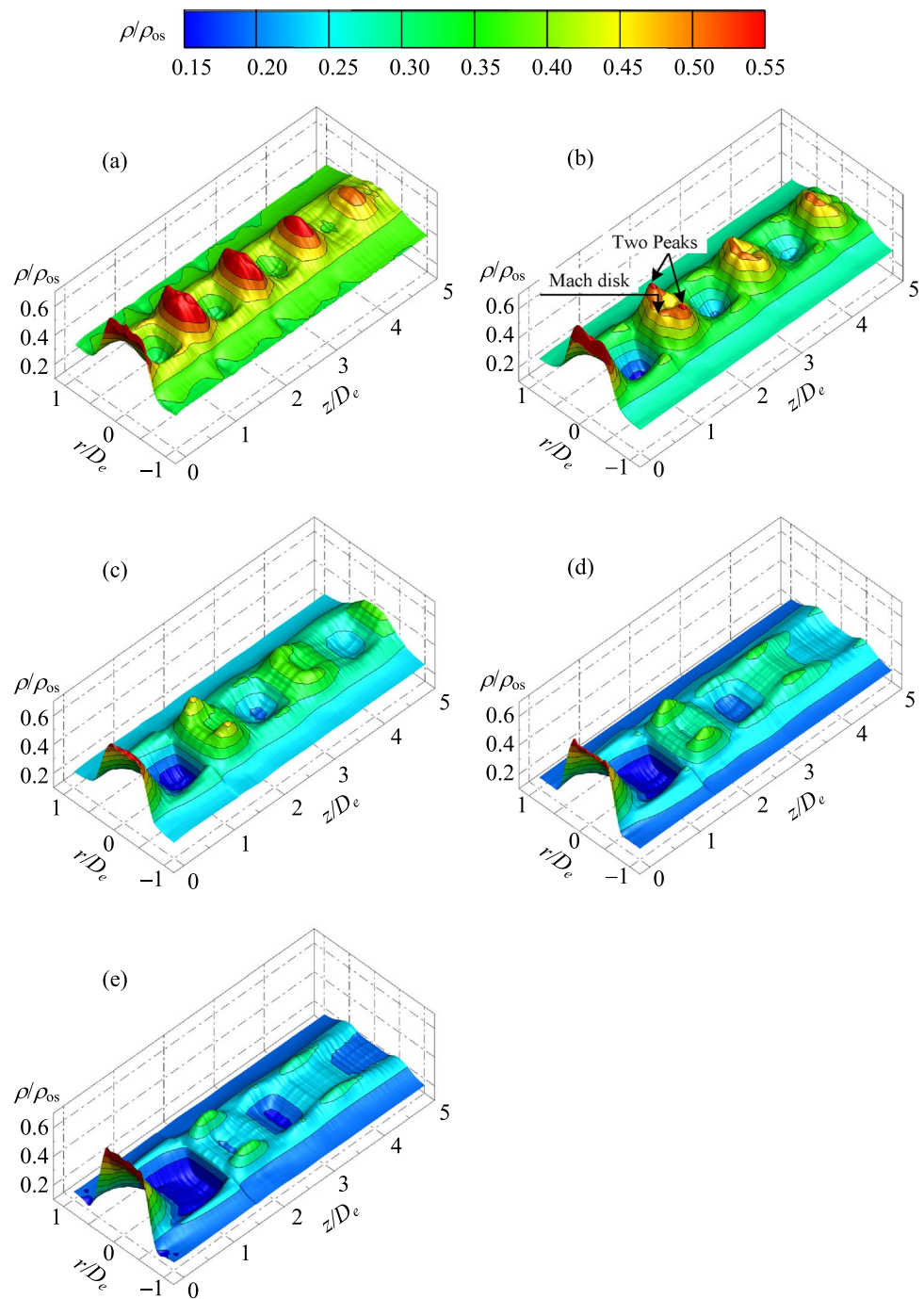
To visually capture the shock structure in the near-field zone from the nozzle exit to the location five times downstream of the nozzle exit diameter, elevated views of the jet density fields were reproduced from Fig. 5, as illustrated in Fig. 6 where the density fields are normalized by the stagnation density ρ_{os} in the plenum chamber upstream of the nozzle, and the density contour level is shown in the color bar at the top of Fig. 6. This representation causes the flow topology of the jet near-field zone to be obvious at a glance. The radial and streamwise distances from the nozzle exit are normalized by the nozzle exit diameter D_e. The density fields of Fig. 6 express statistically averaged fields. It is notable that for the density fields normalized by ρ_{os}, the density fields from the nozzle exit to the end location of the expansion region in the first shock-cell are almost the same regardless of the NPR because the flow is governed by the isentropic process.

As shown in Fig. 6a for NPR = 3, the densities at the nozzle exit gradually decrease toward a downstream valley due to the expansion waves emerging from the nozzle lip and then gradually increase by compression waves that are produced as the reflection of the expansion waves at the jet free boundaries. This situation occurs inside the first shock-cell. A similar phenomenon can be observed in the successive shock-cells following the first shock-cell. For NPR = 4, Fig. 6b shows that a Mach disk appears at the valley as shown by the downward arrow. The Mach disk is characterized by a sharp increase in the density. Two local maxima of the density, which are expressed as the two peaks in Fig. 6b, are produced at both sides radially away from the Mach disk, and they suggest the occurrence of slip streams extending downstream from the triple points of the Mach disk. When the NPR increases from 5 to 7, as shown in Figs. 6c through 6d, the valley becomes deeper to form a strong Mach disk in the first shock-cell. Moreover, the Mach disk diameter increases with an increasing NPR. The flow Mach number just ahead of the Mach disk increases with an increasing NPR.

3.3 Jet centerline density profiles

The effects of the NPR on the density distribution along the jet central axis are shown in Fig. 7. These density distributions represent the flow characteristics along the jet central axis in the two-dimensional density fields of the microjets shown in Fig. 5. The dashed line parallel to the abscissa

Fig. 6 Elevated views of the two-dimensional density fields including the central axis of underexpanded sonic jets for **a** NPR = 3, **b** NPR = 4, **c** NPR = 5, **d** NPR = 6, and **e** NPR = 7. The radial and streamwise distances are normalized by the nozzle exit diameter. The local density is normalized by the stagnation density in the plenum chamber

shown as ρ_j/ρ_b indicates the level of the fully expanded jet density. The red line parallel to the abscissa indicates a level of $\rho/\rho_b = 1.2$, from which the normalized supersonic length L^*/D_e can be determined because the static pressure at the location where the local flow Mach number becomes unity is the same as the ambient pressure p_b. Then, the normalized density ρ^*/ρ_b at the location is maintained constant at 1.2 regardless of the NPR. Therefore, the length along the jet central axis from the nozzle exit to the most downstream location with $\rho/\rho_b = 1.2$ indicates the supersonic length. The

end location of the supersonic region on the jet centerline is shown as the blue short vertical line in Fig. 7a. The same procedure is repeated for all the density fields from Figs. 7b to 7e. The average measurement uncertainties for the density profiles in Fig. 7a through 7e were within 2.2%, 3.4%, 7.3%, 7.1%, and 11.3% of ρ_b, respectively.

As shown in Fig. 7a, the microjet for NPR = 3 includes only weak shocks with almost the same density amplitude and shock-cell length for the first three shock-cells. The density at the nozzle exit gradually decreases with an increasing
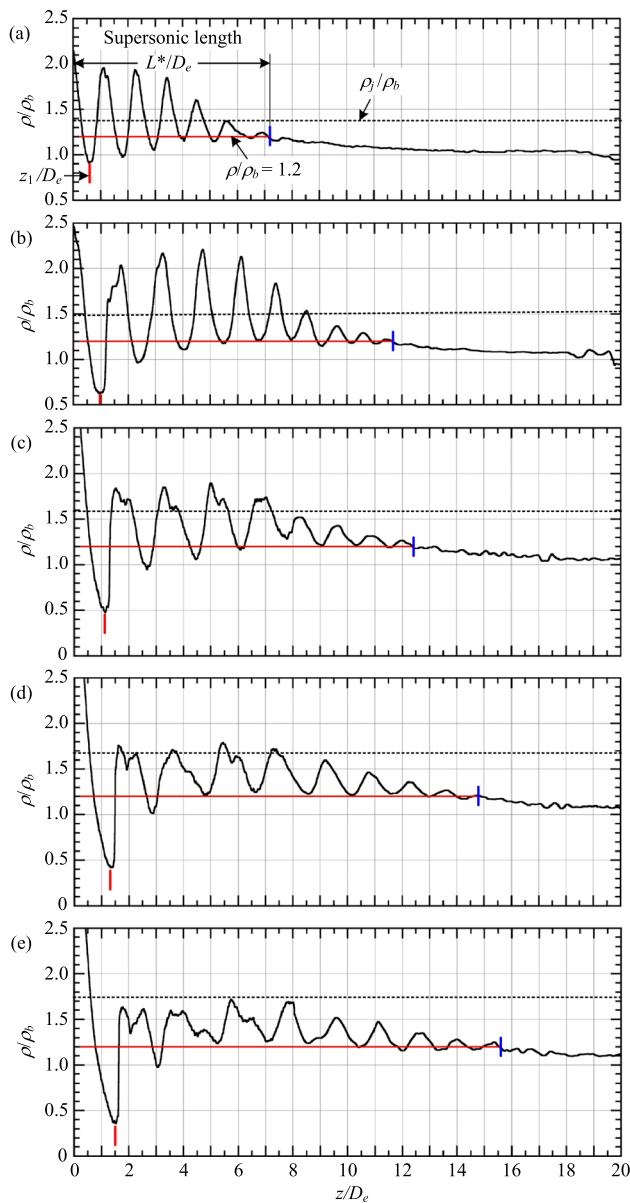
Fig. 7 Density profiles along the jet centerline for a NPR = 3, b NPR = 4, c NPR = 5, d NPR = 6, and e NPR = 7. The abscissa and ordinate are normalized by the nozzle exit diameter and the ambient density, respectively. The red solid line parallel to the abscissa denotes the level of $\rho/\rho_b = 1.2$. The black dashed line indicates the level of the fully expanded jet density normalized by the ambient density. The blue short vertical line shows the end location of the supersonic region. The z_1/D_e with the red short vertical line indicates the normalized streamwise location of the first local minima in the density profile

Fig. 8 Variation in the location of the first density local minimum in the density profile along the jet central axis against the NPR. The open symbols and red solid line denote the experimental data from the present RSD and the corresponding least-squares regression line given by Eq. (8), respectively. The black circular and square symbols show the experimental data captured from the MZI of Sugawara et al. (2020) and Sugawara et al. (2021), respectively. The blue solid line is an empirical curve given by Eq. (9), which shows the Mach disk location for NPRs beyond 3.47

until almost the end of the supersonic region. In addition, the density in the near-field zone where shocks dominate quasi-periodically fluctuates around ρ_j/ρ_b. The local maxima in the density distributions become progressively lower with an increasing NPR. For NPR = 7, the density values inside the microjet are always lower than the level of ρ_j/ρ_b except in the zone near the nozzle exit.

3.4 Flow features in the near-field region

The normalized streamwise location z_1/D_e from the nozzle exit to the minimum value in the density profile along the jet central axis can be determined from Fig. 7 and shown in Fig. 8 as the open symbols against the NPR. The least-squares regression line of the present experimental data is given by

$$\frac{z_1}{D_e} = 0.67\sqrt{\text{NPR} - 1.89} \tag{8}$$

and is shown as the red line in Fig. 8. The present experimental results from RSD are compared with the previous results from MZI shown as the black open and square symbols, which were reproduced by the authors from Sugawara et al. (2020) and Sugawara et al. (2021), respectively.

downstream distance and reaches a minimum value at a location denoted as z_1/D_e with the red short vertical line before increasing with an increasing downstream distance to form the first shock-cell. Similar density variations are repeated by successive shock-cells with gradually decreasing amplitudes of density fluctuations in the downstream direction
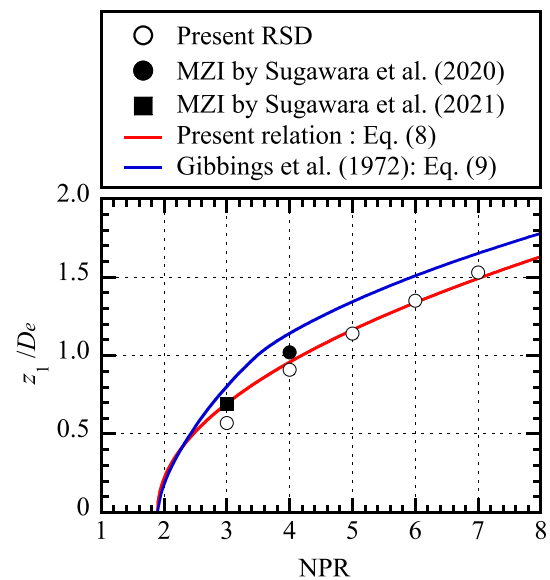
There are some empirical relations for the Mach disk location against the NPR (Franquet et al. 2015). Since a Mach disk is generated at approximately the same location as z_1/D_e if it appears in the first shock-cell, the experimental results for z_1/D_e are compared with the semi-empirical relations proposed in the past about Mach disk locations. Crist et al. (1966) determined a semi-empirical relation that can predict the Mach disk location and showed that the relation is in good quantitative agreement with many experimental data available in the past. Young (1975) analytically derived an approximate relation of the Mach disk location. However, the relations proposed by Crist et al. as well as Young include an assumption that the flow Mach number just upstream of the Mach disk is very large. This implies that their relations are valid for sufficiently large NPRs. Addy (1981) stated that the relation of Crist et al. overestimates Mach disk locations over a range of NPRs from approximately 4 to 8. On the other hand, Gibbings et al. (1972) provided an empirical relation that can be determined based on shadowgraph pictures of jets. In the present study, we compare the experimental results with an empirical relation given by Gibbings et al. (1972) as

$$\frac{z_1}{D_e} = \begin{cases} 0.76(\text{NPR} - 1.893)^{0.61} & \text{for } \text{NPR} < 3.47 \\ 0.84(\text{NPR} - 1.893)^{0.415} & \text{for } \text{NPR} \geq 3.47 \end{cases} \quad (9)$$

Because the relation covers NPRs comparable to those in this study and for NPRs below 3.47, Eq. (9) provides the location of an oblique shock intersection instead of the Mach disk location. The calculation results from Eq. 9 are shown as the blue line in Fig. 8.

As shown in Fig. 8, the empirical curve from Eq. (9) exhibits the same trend as in the present and previous experimental results, but it overestimates the experimental values for all NPRs. For NPRs above approximately 3, the blue line is slightly larger than the red line with the difference kept constant regardless of the NPR. It is notable that the shock captured using the shadowgraph technique is visualized at a location where the second spatial derivative of the density is large, i.e., the shock exists slightly downstream of a location (z_1/D_e) of the local minimum in the density profile because in the density profile for a shock, the location of the maximum second spatial derivative of the density lies between the minima and maxima.

The flow Mach number M_1 at z_1/D_e for a fixed NPR can be estimated using the assumption of isentropic flows from the nozzle inlet to z_1/D_e, and it is shown as the open symbols in Fig. 9. The previous experimental data with the black circular and square symbols by Sugawara et al. (2020, 2021) are also shown in Fig. 9. The red solid line is an approximate curve of the present experimental data given by

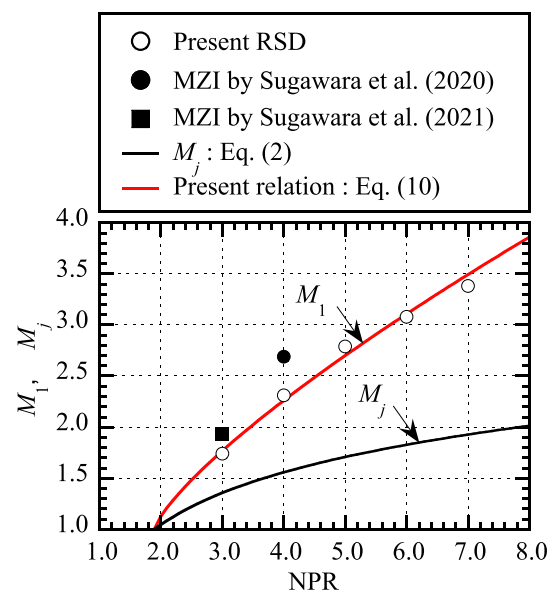$$M = 1 + 0.72\,(\text{NPR} - 1.89)^{0.76} \quad (10)$$

Fig. 9 Variation in the flow Mach number at the first local minimum in the density profile along the jet central axis against the NPR. The open symbols denote the experimental data from the present RSD, and the corresponding least-squared regression line is shown by the red solid line. The black circular and square symbols show the experimental data captured from the MZI of Sugawara et al. (2020) and Sugawara et al. (2021), respectively. The black solid line is the fully expanded flow Mach number given by Eq. (2)

As a reference, the fully expanded flow Mach number M_j from Eq. (2) is represented as the black solid line. Equation (10) is in good agreement with the previous data for NPR =3 without a Mach disk but underestimates for NPR = 4 with a Mach disk. It is noteworthy that M_1, which corresponds to the maximum Mach number in the jet, is much larger than the theoretical Mach number M_j. This indicates that for a given NPR the real flow is extremely expanded.

The jet emerging from the test nozzle is considered to be isentropic flow until just before the shock in the first shock-cell. Based on this assumption, the flow Mach numbers along the jet central axis from the nozzle exit ($z/D_e = 0$) to z_1/D_e can be determined from the density profiles shown in Fig. 7. The results obtained are shown as the five colored solid lines in Fig. 10. The open symbols denote M_1 for each NPR. The five density profiles collapse very well on a single self-similar curve given by

$$M = 1 + 1.58\frac{z}{D_e} \quad (11)$$

The flow Mach number of the jet emerging from the nozzle exit linearly increases from unity at the exit in proportion to the streamwise distance.

Since the jet flow from the nozzle exit to a location just upstream of the shock in the first shock-cell varies according to the isentropic process, flow quantities such as the
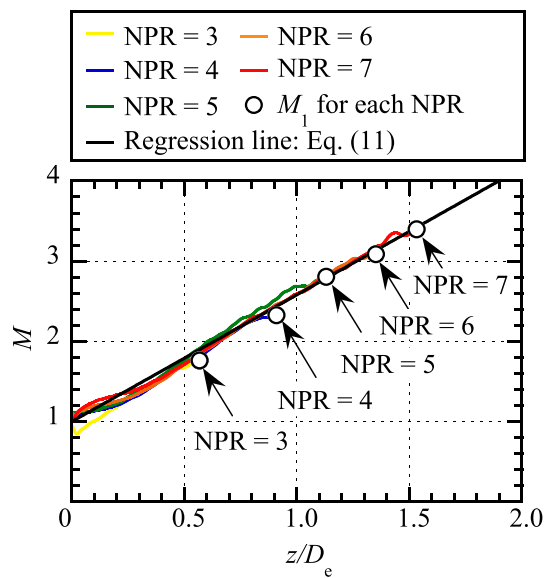
Fig. 10 Variations in the flow Mach numbers from the nozzle exit to the location of the first local minimum in the jet centerline density profile for a fixed NPR. The open symbol at the downstream end of each curve corresponds to the location where the density reaches a minimum. The black line denotes a least-squares regression fitting given by Eq. (11), which was determined from the experimental curves over a range of NPRs from 3 to 7

pressure, density, and temperature can be easily derived from Eq. (11) using isentropic relations. In the past, Crist et al. (1966) proposed an approximate relation that can predict the centerline Mach numbers over a range of NPRs from approximately 10 to 300,000. Equation (11) can be applied to lower NPRs than the equation of Crist et al.

3.5 Supersonic lengths against NPR

We focus on the region far downstream from the nozzle exit. Comparisons between the present and previous results for the normalized supersonic length L^*/D_e of underexpanded microjets emerging from round convergent nozzles are represented against the NPR with M_j in Fig. 11. The black circular and black triangular symbols show the previous experimental data performed by Phalnikar et al. (2008) for round convergent nozzles with exit diameters of $D_e = 200$ μm and 400 μm, respectively. Moreover, the corresponding empirical relation is given by Eq. (6), which is shown as the red solid line. The open circular symbols with the precision error bars show the present experimental results from RSD for the microjets emerging from a round convergent nozzle with a diameter of 1000 μm at the exit. The black and blue solid lines indicate empirical curves given by Eqs. (5) and (7), respectively, which are determined using the experimental data from the Pitot probe surveys. Notably Eq. (6) relates to microscale jets, while Eqs. (5) and (7) to macroscale jets.
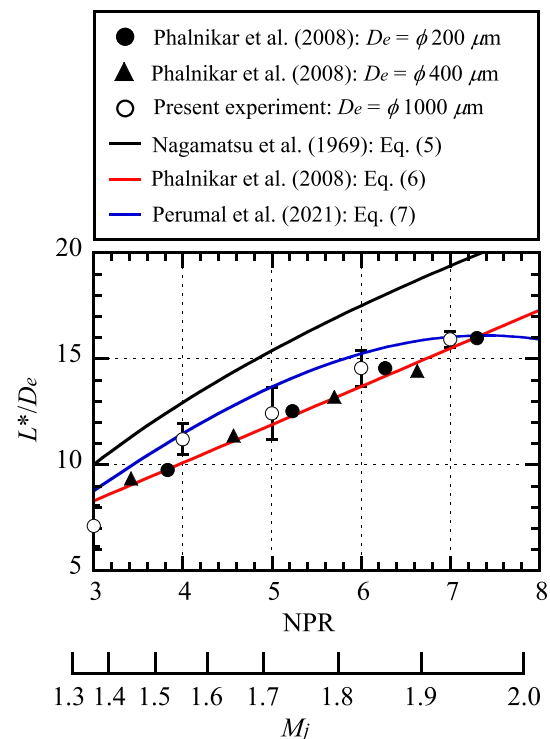

Fig. 11 Comparison of experiments and empirical relations for normalized supersonic lengths of underexpanded microjets. The solid circular and triangular symbols represent the experimental data obtained from the Pitot probe surveys by Phalnikar et al. (2008) using round convergent nozzles with $D_e = 200$ μm and 400 μm, respectively. The open symbols denote the experimental data obtained from the present RSD using a round convergent nozzle with $D_e = 1000$ μm, which are represented with the precision error bars. The black, red, and blue solid lines indicate the empirical relations of Nagamatsu et al. (1969), Phalnikar et al. (2008), and Perumal et al. (2021), respectively. The relation of Phalnikar et al. was derived from experimental data on microscale jets

The L^*/D_e from the empirical relation of Eq. (5) qualitatively shows the same trend as the experimental values of the present and Phalnikar et al. (2008), but it overestimates over all NPRs. Moreover, the deviation gradually increases as the NPR increases. Notably, Eq. (5) was estimated from the various experimental data over a design Mach number range of 1.0 to 2.5 and some total temperatures. Therefore, the major difference between the empirical curve and the experimental data is that Eq. (5) includes experimental data for jets from nozzles with design Mach numbers greater than one. On the other hand, the present experimental data were acquired from cold underexpanded sonic jets only where the total temperature T_{os} in the plenum chamber is equal to the ambient temperature, T_b.

The approximate curve determined from Eq. (6) is proportional to the NPR, while the present experimental data vary like an upward convex parabola with respect to the NPR. However, a good quantitative agreement is reached

between Eq. (6) and the present results. The L^*/D_e estimated from Eq. (7) exhibits a smooth convex curve, which increases first with an increase in the NPR and then gradually remains constant after NPR is approximately 6.5. It is in good quantitative agreement with the present experimental data except for NPRs = 3 and 5, but slightly overestimates the experimental data of Phalnikar et al. for NPRs below approximately 6.5. Considering that Eqs. (6) and (7) were determined from Pitot probe measurements, RSD and Pitot prove surveys are comparable to measurements of the supersonic length. However, we highlight that the Pitot probe surveys can obtain the experimental data by traversing the probe within the flow field of interest. Moreover, it includes shock-losses in supersonic regions, while the RSD makes it possible to nonintrusively capture the genuine full density field of the flow within the field of view with a high spatial resolution.

3.6 RSD versus MZI

There are no theoretical solutions available that predict the entire flow features of an underexpanded jet, including strong shocks such as a Mach disk. Even currently, Pitot tubes have been utilized to investigate the shock structures within the near-field zone of microjets (Phalnikar et al. 2008; Aniskin et al. 2013, 2015; Mironov et al. 2019). However, Pitot probe measurements within the shock-containing jet have the potential to provide significant measurement errors due to shock-prove interference (Saddington et al. 2004). In addition, Mironov et al. (2019) demonstrated that the Pitot pressure profile along the centerline of an axisymmetric underexpanded microjet is shifted in the downstream direction with respect to the curves that are calculated for free microjets. Numerical solutions such as the Reynolds-averaged Navier–Stokes (RANS) simulations are also greatly influenced by the mesh size and shape, the code, turbulence models, etc. Computational results are usually validated by comparing them with experimental data. Therefore, it is important to compare physical quantities measured by different kinds of facilities under the same experimental conditions to ensure the reliability of the experimental data.

Quantitative comparisons between the RSD and MZI for the three representative density profiles of shock-containing microjets for NPR = 3 are shown in Fig. 12 where Fig. 12a, b, and c denotes the density profiles along the jet centerline ($r/D_e = 0$), intermediate line ($r/D_e = 0.25$), and lipline ($r/D_e = 0.5$), respectively. The abscissa is the streamwise distance from the nozzle exit normalized by D_e. The ordinate is the local density normalized by ρ_{os}. The leftward arrow on each ordinate in Fig. 12a and b indicates the theoretical value at the nozzle exit that can be estimated based upon the assumption of isentropic flows from the nozzle inlet to the exit. The density profiles from the MZI are reproduced from
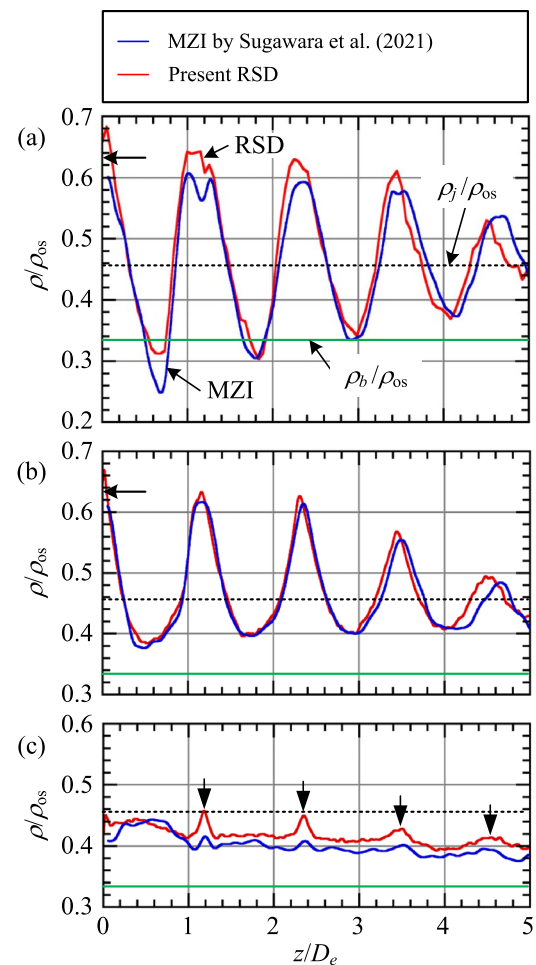

Fig. 12 Comparison of the RSD and MZI for three-representative streamwise density profiles along the **a** jet centerline ($r/D_e = 0$), **b** intermediate line ($r/D_e = 0.25$), and **c** lipline $r/D_e = 0.5$ under NPR = 3. The red and blue lines denote the density profiles from the present RSD and the MZI of Sugawara et al. (2021), respectively. The leftward arrow on the ordinate shows the theoretical density ratio at the nozzle exit plane estimated based upon the assumption of isentropic flow from the nozzle inlet to the exit. The green horizontal and black dashed lines are the ambient density and the fully expanded jet density, respectively, normalized by the plenum density

Sugawara et al. (2021) by the authors. The measurement uncertainties for the present RSD were omitted to make the experimental curves easier to read where density values were acquired within an average uncertainty of 0.74% for the stagnation density ρ_{os} in the plenum chamber.

As shown in Fig. 12a, a comparison between the density profiles along the jet central axis from RSD and MZI indicates that there is very little difference in terms of both shock-cell spacings and wave variations on the first three shock-cells except that the results from the RSD have slightly higher density maxima as well as lower density minimum within the first shock-cell when compared with those from MZI. Regarding the fourth shock-cell, the

agreement is not as good. Both density profiles oscillate quasi-periodically around ρ_j/ρ_{os} with gradually decreasing the amplitude in the flow direction.

Regarding the density profile along the intermediate line, Fig. 12b demonstrates that the results from RSD and MZI agree quantitatively very well with each other except for the fourth shock-cell. In addition, the density minima are nearly constant in the flow direction, while the maxima gradually decrease in the flow direction. The density minima are always higher than the level of ρ_b/ρ_{os}.

Figure 12c shows that the density profiles along the lipline from the RSD and MZI are included between the levels of ρ_j/ρ_{os} and ρ_b/ρ_{os}. In addition, both density profiles exhibit significant small bumps appearing quasi-periodically, which are marked as downward arrows. These bumps are responsible for the reflection as expansion waves of weak oblique shocks at the jet free boundaries (Sugawara et al. 2021). The density profile from the RSD is slightly higher than that from the MZI.

Regarding shock-containing microjets for NPR = 4, a quantitative comparison similar to Fig. 12 is made, as shown in Fig. 13. The density profiles from the MZI were reproduced from Sugawara et al. (2020) by the authors. The measurement uncertainties for the present RSD were within an average uncertainty of 0.85% for ρ_{os}. Figure 13a shows that the density profiles along the jet central axis from the RSD and MZI capture a Mach disk at $z/D_e =$ approximately 1.2. The density profile from the RSD coincides very well with that from the MZI between the nozzle exit and a location just upstream of the Mach disk. The flow in this zone can be regarded as approximately isentropic.

In addition, there is good quantitative agreement between both density profiles except that the density variations immediately before and after each shock in the first and second shock-cells are slightly different between both methods. Both techniques have almost the same spatial resolution of approximately 4 μm in Fig. 13. Therefore, the slight difference between the RSD and MZI is perhaps partly due to the experimental techniques employed and partly due to the differences in the proficiency of the researchers. Figure 13b and 13c shows that the density profiles along the intermediate line and lipline from the RSD and MZI are in extremely good agreement with each other with regard to the spacing, amplitude, and geometrical shape.

The experimental results of Figs. 12 and 13 are useful, providing detailed benchmark data for other measurement techniques to measure the density fields of microscale and macroscale supersonic free jets. In addition, they provide a wealth of useful data for the validation of computational codes.
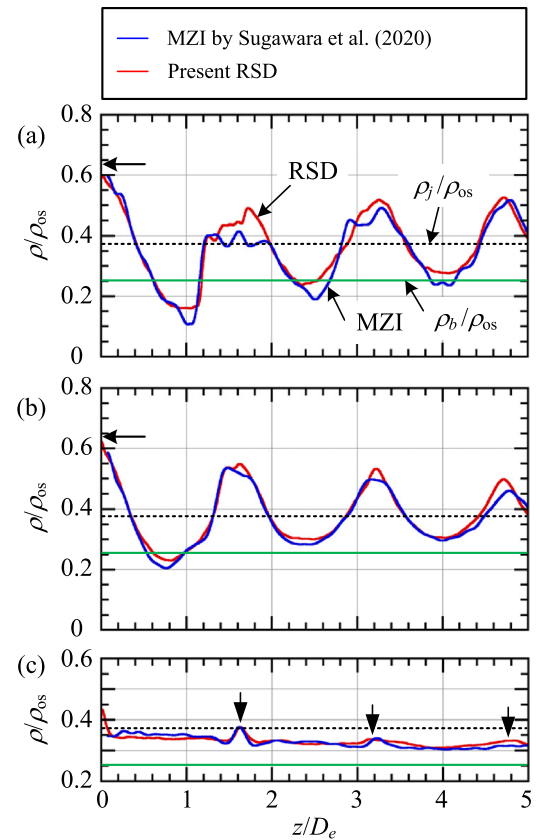

Fig. 13 Comparison of the RSD and MZI for three-representative streamwise density profiles along the **a** jet centerline ($r/D_e = 0$), **b** intermediate line ($r/D_e = 0.25$), and **c** lipline $r/D_e = 0.5$ under NPR = 4. The red and blue lines denote the density profiles from the present RSD and the MZI of Sugawara et al. (2020), respectively. The leftward arrow on the ordinate shows the theoretical density ratio at the nozzle exit plane estimated based upon the assumption of isentropic flow from the nozzle inlet to the exit. The green horizontal and black dashed lines are the ambient density and the fully expanded jet density, respectively, normalized by the plenum density

4 Concluding remarks

In this study, RSD was applied for underexpanded microjets emerging from a round convergent nozzle with an exit diameter of $D_e = 1$ mm to quantitatively visualize an extensive region from the nozzle exit to 20 D_e downstream. The experiments were performed over a range of NPRs from 3.0 to 7.0 in steps of 1.0, and the three-dimensional density fields of the microjets were reconstructed at a spatial resolution of approximately 4 μm through the Abel inversion method based upon the assumption of axisymmetric flows. The three-dimensional spatial evolution of the shock structure in the near-field region of the underexpanded microjet was demonstrated with an elevated view, and the effects of the NPR on the shock structure were clarified.

The normalized streamwise location z_1/D_e of the first local minimum in the jet centerline density profile was

experimentally provided against the NPR and compared with the experimental data from the MZI as well as the previous empirical relation given by Eq. (9) for the Mach disk location. In addition, the maximum Mach number M_1 in underexpanded microjets, which occurs at z_1, was represented by Eq. (10) as a function of the NPR and compared with the previous experimental data from the MZI. Furthermore, the flow Mach number from the nozzle exit to z_1/D_e was provided as an empirical relation given by Eq. (11).

The supersonic length L^*, which is defined as the distance along the jet central axis from the nozzle exit to the location farthest downstream at which there exists a local flow Mach number of unity, was acquired from the density profile along the jet central axis for each NPR. The normalized supersonic length L^*/D_e from the RSD was quantitatively compared with the empirical curves from Eqs. (5), (6), and (7). It was found that Eq. (5) overestimates the present experimental results over all the NPRs, while Eqs. (6) and (7) relatively provide accurate results.

Quantitative comparisons between the RSD and MZI for the three representative density profiles along the jet centerline, intermediate line, and lipline between the nozzle exit and $5D_e$ downstream were made for the first time, where the same convergent nozzle with an exit diameter of $D_e = 1$ mm was used in both experiments for NPRs of 3.0 and 4.0. It was shown that the density profiles from both techniques are in good quantitative agreement with each other in terms of the shock-cell spacing, density amplitude, and wave shape. However, a slight difference was observed between the RSD and MZI in the density profiles just ahead and behind the Mach disk. At this time, we are unable to determine the cause of the discrepancy. A quantitative comparison with other measurement techniques is desired.

It should be noted that the conventional schlieren and shadowgraph methods are the line-of-sight techniques; thus, the first and second spatial derivatives of the density for the schlieren and shadowgraph techniques, respectively, are integrated along the entire optical path length, offering a two-dimensional representation of a three-dimensional flow field. Moreover, the RSD can easily capture three-dimensional density fields of shock-containing microjets in an extensive area from the nozzle exit to a location tens of times greater than the nozzle exit diameter. We emphasize the need for detailed experimental data on microjets with a strong shock. These are the first reported measurements of supersonic lengths of shock-containing jets emerging from round nozzles using the RSD. The RSD produces repeatable datasets that can be available for validation of numerical simulations of supersonic microjets and could have the potential to study various flow features that occur in high-speed flows. However, at this stage, no clear conclusions have been reached regarding the effects of viscosity on the flow structure of the microjet emerging from the nozzle used in this study. This

issue will be clarified in the future through a combination of experiments and numerical calculations.

Declarations

Conflict of interest The authors report no conflict of interest.

Ethical approval Not applicable.

References

Addy AL (1981) Effects of axisymmetric sonic nozzle geometry on Mach disk characteristics. AIAA J 19:121–122

Agrawal AK, Wanstall CT (2018) Rainbow schlieren deflectometry for scalar measurements in fluid flows. J Flow Vis Image Process 25:329–357

Al-Ammar K, Agrawal AK, Gollahalli SR, Griffin D (1998) Application of rainbow schlieren deflectometry for concentration measurements in an axisymmetric helium jet. Exp Fluids 25:89–95

Alkislar MB, Krothapalli A, Butler GW (2007) The effect of streamwise vortices on the aeroacoustics of a Mach 0.9 jet. J Fluid Mech 578:139–169

Aniskin V, Mironov S, Maslov A (2013) Investigation of the structure of supersonic nitrogen microjets. Microfluid Nanofluidics 14:605–614

Aniskin VM, Mironov SG, Maslov AA, Tsyryulnikov IS (2015) Supersonic axisymmetric microjets: structure and laminar-turbulent transition. Microfluid Nanofluidics 19:621–634

Crist S, Sherman PM, Glass DR (1966) Study of the highly underexpanded sonic jet. AIAA J 4:68–71

Donaldson CD, Snedeker RS (1971) A study of free jet impingement. Part 1. Mean properties of free and impinging jets. J Fluid Mech 45:281–319

Edgington-Mitchell D, Honnery DR, Soria J (2014) The underexpanded jet Mach disk and its associated shear layer. Phys Fluids 26:096101

Feng T, McGuirk JJ (2016) Measurements in the annular shear layer of high subsonic and under-expanded round jets. Exp Fluids 57:7

Franquet E, Perrier V, Gibout S, Bruel P (2015) Free underexpanded jets in a quiescent medium: a review. Prog Aerosp Sci 77:25–53

Fukunaga R, Ezoe M, Nakao S, Miyazato Y (2022) Application of rainbow schlieren tomography for shock-containing rectangular jets. J Vis 25:687–695

Gibbings JC, Ingham J, Johnson D (1972) Flow in a supersonic jet expanding from a convergent nozzle, Technical Report, Aeronautical Research Council, C.P.No. 1197

Greenberg PS, Klimek RB, Buchele DR (1995) Quantitative rainbow schlieren deflectometry. Appl Opt 34:3810–3825

Gribben BJ, Badcock KJ, Richards BE (2000) Numerical study of shock-reflection hysteresis in an underexpanded jet. AIAA J 38:275–283

Hileman JI, Samimy M (2006) Mach number effects on jet noise sources and radiation to shallow angles. AIAA J 44:1915–1918

Hornung HG (2000) Oblique shock reflection from an axis of symmetry. J Fluid Mech 409:1–12

Hornung HG, Schwendeman DW (2001) Oblique shock reflection from an axis of symmetry: shock dynamics and relation to the Guderley singularity. J Fluid Mech 438:231–245

Kaushik M (2019) Theoretical and experimental aerodynamics, 1st edn. Springer

Kolhe PS, Agrawal AK (2009) Density measurements in a supersonic microjet using miniature rainbow schlieren deflectometry. AIAA J 47:830–838

Kumar V, Alvi FS (2006) Use of high-speed microjets for active separation control in diffusers. AIAA J 44:273–281

Lau JC, Morris PJ, Fisher MJ (1979) Measurements in subsonic and supersonic free jets using a laser velocimeter. J Fluid Mech 93:1–27

Louwerse MC, Jansen HV, Groenendijk MNW, Elwenspoek MC (2009) Nozzle fabrication for micropropulsion of a microsatellite. J Micromech Microeng 19:045008

Love ES, Grigsby CE, Lee LP, Woodling MJ (1959) Experimental and theoretical studies of axisymmetric free jets, NASA TR, R-6

Maeda H, Fukuda H, Kubo K, Nakao S, Ono D, Miyazato Y (2018) Structure of underexpanded supersonic jets from axisymmetric Laval nozzles. J Flow Vis Image Process 25:33–46

Mironov SG, Aniskin VM, Korotaeva TA, Tsyryulnikov IS (2019) Effect of the Pitot tube on measurements in supersonic axisymmetric underexpanded microjets. Micromachines 10:235

Morrison GL, McLaughlin DK (1980) Instability process in low Reynolds number supersonic jets. AIAA J 18:793–800

Muraoka R, Hiejima T (2022) Onset conditions for Mach disk formation in underexpanded jet flows. Phys Fluids 34:116125

Nagamatsu HT, Sheer Jr. RE, Horvay G (1969) Supersonic jet noise theory and experiments, NASA SP-207, 17-51

Nagata T, Islam MM, Miyaguni T, Nakao S, Miyazato Y (2022) Shock-cell spacings of underexpanded sonic jets emerging from elliptic nozzles. Exp Fluids 63:111

Nazari AZ, Ishino Y, Ishiko Y, Ito F, Kondo H, Yamada R, Motohiro T, Miyazato Y, Nakao S (2020) Multi-schlieren CT measurements of supersonic microjets from circular and square micro nozzles. J Flow Control Meas Visual 8:77–101

Perumal AK, Rathakrishnan E (2021) Scaling law for supersonic core length in circular and elliptic free jets. Phys Fluids 33:051707

Phalnikar KA, Kumar R, Alvi FS (2008) Experiments on free and impinging supersonic microjets. Exp Fluids 44:819–830

Powell A (1988) The sound-producing oscillations of round underexpanded jets impinging on normal plates. J Acoust Soc Am 83:515–533

Rathakrishnan E (2019) Applied gas dynamics, 2nd edn. John Wiley & Sons

Saad MA (1993) Compressible fluid flow, 2nd edn. Prentice Hall, pp 157–158

Saddington AJ, Lawson NJ, Knowles K (2004) An experimental and numerical investigation of under-expanded turbulent jets. Aeronaut J 108:145–152

Sakurai T, Handa T, Koike S, Mii K, Nakano A (2015) Study on the particle traceability in transonic and supersonic flows using molecular tagging velocimetry. J Vis 18:511–520

Scroggs SD, Settles GS (1996) An experimental study of supersonic microjets. Exp Fluids 21:401–409

Settles GS (2001) Schlieren and shadowgraph techniques: Visualizing phenomena in transparent media, 1st edn. Springer, Berlin

Shirie JW, Seubold JG (1967) Length of the supersonic core in high-speed jets. AIAA J 5:2062–2064

Smedley GT, Phares DJ, Flagan RC (1999) Entrainment of fine particles from surfaces by gas jets impinging at normal incidence. Exp Fluids 26:324–334

Sugawara S, Nakao S, Miyazato Y, Ishino Y, Miki K (2020) Three-dimensional reconstruction of a microjet with a Mach disk by Mach-Zehnder interferometers. J Fluid Mech 893:A25

Sugawara S, Nakao S, Miyazato Y, Ishino Y, Miki K (2021) Quantitative flow visualization of slightly underexpanded microjets by Mach-Zehnder interferometers. Flow Turbul Combust 106:971–992

Takano H, Kamikihara D, Ono D, Nakao S, Yamamoto H, Miyazato Y (2016) Three-dimensional rainbow schlieren measurements in underexpanded sonic jets from axisymmetric convergent nozzles. J Therm Sci 25:78–83

Tam CKW (1995) Supersonic jet noise. Annu Rev Fluid Mech 27:17–43

Tam CKW, Tanna HK (1982) Shock associated noise of supersonic jets from convergent-divergent nozzles. J Sound Vib 81:337–358

Wernet MP (2016) Application of tomo-PIV in a large-scale supersonic jet flow facility. Exp Fluids 57:1–24

Young WS (1975) Derivation of the free-jet Mach-disk location using the entropy-balance principle. Phys Fluids 18:1421–1425

Yüceil KB (2017) A comparison of PIV and interferometric Rayleigh scattering measurements in the near field of underexpanded sonic jets. Aerosp Sci Technol 67:31–40